

Spectral-domain spectrally-encoded endoscopy

Dvir Yelin, W. Matthew White, Jason. T. Motz, Seok H. Yun, and Brett E. Bouma

*Harvard Medical School and the Wellman Center for Photomedicine, Massachusetts General Hospital,
55 Fruit Street, BAR 703, Boston, Massachusetts 02114
dyelin@partners.org*

Guillermo J. Tearney

*Harvard Medical School, Wellman Center for Photomedicine, and the Pathology Department, Massachusetts
General Hospital, 55 Fruit Street, BAR 703, Boston, Massachusetts 02114*

Abstract: Spectrally-encoded miniature endoscopy uses a single optical fiber and wavelength division multiplexing to obtain macroscopic images through miniature, flexible probes. In turn, it has the potential to enable two- and three-dimensional imaging within the body at locations that are currently difficult to access with conventional endoscopes. Here we present a novel detection scheme for spectrally-encoded endoscopy using spectral-domain interferometry. Compared to previous time-domain configurations, this new detection method results in greater than 1000-fold increase in sensitivity (77 dB), a 6-fold increase in imaging speed (30 volumes per second), and a 2-fold increase in depth range (2.8 mm). We demonstrate spectrally-encoded, spectral-domain detection by conducting video-rate, three-dimensional imaging in a variety of specimens, including the paws of a mouse embryo and excised human ear bones. Our results show that this new technology enables video rate spectrally-encoded endoscopy and will therefore be useful for a variety of minimally invasive medical applications.

©2007 Optical Society of America

OCIS codes: (170.2150) Endoscopic imaging; (170.6900) Three-dimensional microscopy; (110.1650) Coherence imaging; (170.4580) Optical diagnostics for medicine.

References and links

1. B. I. Hirschowitz, "Endoscopic examination of the stomach and duodenal cap with the fiberscope," *Lancet* **1**, 1074-1078 (1961).
2. F. Ishibashi, K. Aziz, G. S. Abela, and S. Waxman, "Update on Coronary Angioscopy: Review of a 20-year experience and potential application for detection of vulnerable plaque," *J. Interv. Cardio.* **19**, 17-25 (2006).
3. V. R. Jacobs, M. Kiechle, B. Plattner, T. Fischer, and S. Paepke, "Breast ductoscopy with a 0.55-mm mini-endoscope for direct visualization of intraductal lesions," *J Minim Invasive Gynecol* **12**, 359-364 (2005).
4. T. Matsunaga, Y. Kawakami, K. Namba, and M. Fujii, "Intraductal biopsy for diagnosis and treatment of intraductal lesions of the breast," *Cancer* **101**, 2164-2169 (2004).
5. E. A. Reece, "First trimester prenatal diagnosis: Embryoscopy and fetoscopy," *Sem. Perinat.* **23**, 424-433 (1999).
6. C. M. Brown, P. G. Reinhall, S. Karasawa, and E. J. Seibel, "Optomechanical design and fabrication of resonant microscanners for a scanning fiber endoscope," *Opt. Eng.* **45**, 043001 (2006).
7. D. L. Dickensheets and G. S. Kino, "Micromachined scanning confocal optical microscope," *Opt. Lett.* **21**, 764-766 (1996).
8. A. L. Polglase, W. J. McLaren, S. A. Skinner, R. Kiesslich, M. F. Neurath, and P. M. Delaney, "A fluorescence confocal endomicroscope for in vivo microscopy of the upper- and the lower-GI tract," *Gastro. Endosc.* **62**, 686-695 (2005).
9. G. J. Tearney, M. Shishkov, and B. E. Bouma, "Spectrally encoded miniature endoscopy," *Opt. Lett.* **27**, 412-414 (2002).
10. G. J. Tearney, S. A. Boppart, B. E. Bouma, M. E. Brezinski, N. J. Weissman, J. F. Southern, and J. G. Fujimoto, "Scanning single-mode fiber optic catheter-endoscope for optical coherence tomography," *Opt. Lett.* **21**, 543-545 (1996).
11. D. Yelin, B. E. Bouma, N. Iftimia, and G. J. Tearney, "Three-dimensional spectrally encoded imaging," *Opt. Lett.* **28**, 2321-2323 (2003).

12. L. Froehly, S. N. Martin, T. Lasser, C. Depeursinge, and F. Lang, "Multiplexed 3D imaging using wavelength encoded spectral interferometry: a proof of principle," *Opt. Commun.* **222**, 127-136 (2003).
13. D. Yelin, S. H. Yun, B. E. Bouma, and G. J. Tearney, "Three-dimensional imaging using spectral encoding heterodyne interferometry," *Opt. Lett.* **30**, 1794-1796 (2005).
14. D. Yelin, I. Rizvi, W. M. White, J. T. Motz, T. Hasan, B. E. Bouma, and G. J. Tearney, "Three-dimensional miniature endoscopy," *Nature* **443**, 765-765 (2006).
15. G. J. Tearney, B. E. Bouma, and J. G. Fujimoto, "High-speed phase- and group-delay scanning with a grating-based phase control delay line," *Opt. Lett.* **22**, 1811-1813 (1997).
16. M. Wojtkowski, A. Kowalczyk, R. Leitgeb, and A. F. Fercher, "Full range complex spectral optical coherence tomography technique in eye imaging," *Opt. Lett.* **27**, 1415-1417 (2002).
17. C. Klug, B. Fabinyi, and M. Tschabitscher, "Endoscopy of the middle ear through the Eustachian tube: Anatomic possibilities and limitations," *Am. J. Otol.* **20**, 299-303 (1999).
18. O. D. Almeida, "Current state of office laparoscopic surgery," *J. Am. Assoc. of Gynecol. Laparosc.* **7**, 545-546 (2000).
19. J. R. Feste, "Use of optical catheters for diagnostic office laparoscopy," *J. Reprod. Med.* **41**, 307-312 (1996).
20. P. N. Fuller, "Microendoscopic surgery: A comparison of four microendoscopes and a review of the literature," *Am. J. Obstet. Gynecol.* **174**, 1757-1761 (1996).
21. O. Nahlili and A. M. Baruchin, "Sialoendoscopy: three years' experience as a diagnostic and treatment modality," *J. Oral Maxillofac. Surg.* **55**, 912-918; discussion 919-920 (1997).
22. S. Rimbach, G. Bastert, and D. Wallwiener, "Technical results of fallopscopy for infertility diagnosis in a large multicentre study," *Human Reprod.* **16**, 925-930 (2001).
23. N. Fujita, Y. Noda, G. Kobayashi, K. Kimura, and K. Ito, "Endoscopic approach to early diagnosis of pancreatic cancer," *Pancreas* **28**, 279-281 (2004).
24. T. Philipp, W. Feichtinger, M. I. Van Allen, E. Separovic, A. Reiner, and D. K. Kalousek, "Abnormal embryonic development diagnosed embryoscopically in early intrauterine deaths after in vitro fertilization: a preliminary report of 23 cases," *Fertil. Steril.* **82**, 1337-1342 (2004).
25. M. V. Senat, J. Deprest, M. Boulvain, A. Paupe, N. Winer, and Y. Ville, "Endoscopic laser surgery versus serial amnioreduction for severe twin-to-twin transfusion syndrome," *New Eng. J. Med.* **351**, 136-144 (2004).
26. G. Cinalli, P. Cappabianca, R. de Falco, P. Spennato, E. Cianciulli, L. M. Cavallo, F. Esposito, C. Ruggiero, G. Maggi, and E. de Divitiis, "Current state and future development of intracranial neuroendoscopic surgery," *Expert Rev. Med. Dev.* **2**, 351-373 (2005).
27. C. Schizas, E. Tziridis, and J. Saksena, "Microendoscopic discectomy compared with standard microsurgical discectomy for treatment of uncontained or large contained disc herniations," *Neurosurgery* **57**, 357-360; discussion 357 - 360 (2005).
28. A. J. Saltzman and S. Waxman, "Angioscopy and ischemic heart disease," *Curr. Opin. Cardiol.* **17**, 633 - 637 (2002).
29. D. Yelin, B. E. Bouma, S. H. Yun, and G. J. Tearney, "Double-clad fiber for endoscopy," *Opt. Lett.* **29**, 2408 - 2410 (2004).
30. J. T. Motz, D. Yelin, B. J. Vakoc, B. E. Bouma, and G. J. Tearney, "Spectral- and frequency-encoded fluorescence imaging," *Opt. Lett.* **30**, 2760-2762 (2005).

1. Introduction

Clinical procedures that rely on endoscopes and laparoscopes have been on the rise for several decades. By making procedures less invasive, devices for imaging inside the body reduce complications, recovery time, and cost. The number of endoscopic and laparoscopic applications is capped in part by the size and flexibility of conventional devices, which limit the settings where they can be performed. Also missing is three-dimensional (3D) information, which may be important for diagnosis and is especially useful when conducting surgical operations in confined spaces that can only be accessed by small instruments.

The first endoscope was an optical fiber bundle, invented in 1957 by Lawrence Curtiss, Wilbur Peters, and Basil Hirschowitz [1]. By allowing physicians to see inside the body, this invention forever changed the face of medical practice. While larger endoscopes now employ solid state CCD cameras for superior image quality, miniature endoscopes still use bundles of optical fibers to transmit a two-dimensional image.

Fiber bundle endoscopes with sub-millimeter diameters have been used for a variety of clinical applications. [2-5]. However, maintaining good image quality at such small diameters is challenging: each optical fiber, including its cladding, has a finite diameter and only a limited number of optical fibers can be packed into a confined space. The cladding itself is also a problem, as it does not transmit image data and typically results in a honeycomb pattern superimposed on the image (pixelation artifact). The limitations of fiber bundles for miniature

endoscopic imaging have motivated the search for other methods. Image formation with a single optical fiber is particularly attractive since this approach provides flexible access while maintaining excellent light transmission. Single-fiber probes have been demonstrated using a MEMS scanner mounted at the distal end of a single-mode fiber [6, 7]. Previous work has also demonstrated that an optical fiber can be driven by a piezoelectric crystal so that its oscillations result in 2D scanning of a focused beam on the sample [8]. While beautiful images, devoid of pixelation artifacts, have been obtained using these techniques, the size of the scanning mechanisms make their use in the smallest ($\leq 350 \mu\text{m}$ diameter) endoscopes difficult.

Spectrally-encoded endoscopy (SEE) [9] is a recently developed, single fiber miniature endoscopy technique that takes a different approach. With SEE, polychromatic light emanating from a fiber is encoded by color (wavelength) and each wavelength is projected onto a distinct location of the tissue surface. Using a spectrometer, light reflected from the patient is decoded outside the body to form one dimension of the endoscopic image. By rotating the probe, a second dimension can be scanned and a 2D image can be generated. Since a scanning mechanism is not required within the endoscope, the diameter of the SEE probe can be as small as that of the optical fiber, which is typically in the range of 80-250 μm . Furthermore, the number of pixels in an SEE image can be larger than that of fiber bundles, dependent only on the spectral width of the light source and the ability of the probe to separate out the different wavelength components.

In practice, a single line of different wavelengths is projected onto the sample by using a diffraction grating and an imaging lens at the distal tip of the miniature endoscope. The number of resolvable points⁹ along this line is given by:

$$N_x = \frac{\Delta\lambda \cdot G \cdot D}{\lambda \cdot \cos \theta}, \quad (1)$$

where λ denotes the central wavelength, $\Delta\lambda$ the source total bandwidth, G the grating's groove density, D the beam diameter, and θ denotes Littrow's angle. A two-dimensional image is formed by scanning this spectrally-encoded line by rotating the fiber using well-established mechanical transduction mechanisms, such as a motor or a galvanometer affixed to the proximal end of the fiber. These scanners, which need only operate at a repetition rate of 10-30 Hz for video imaging, do not add size to the portion of the probe that comes into contact with the patient, as they are located outside the body. [10]

Spectral encoding technology is not limited to two-dimensional endoscopy. When the grating and lens are placed in one arm of an optical interferometer depth information can also be obtained. Proof-of-principle, 3D imaging of inanimate objects has been reported using spectral encoding with a variety of interferometric techniques, including speckle pattern subtraction, [11] and time- and spectral-domain heterodyne interferometry. [12, 13]

In a recent communication [14] we reported the first demonstration of SEE through a miniature fiber optic probe. The 350 μm diameter probe was delivered into the peritoneal cavity of a living mouse through a modified hypodermic needle and 3D images of sub-millimeter tumor nodules were obtained at video rates. In this paper we describe in detail the novel spectral-domain interferometry technology that enables 3D video rate SEE imaging. Additionally, we present a signal-to-noise (SNR) analysis for both time- and spectral-domain SEE.

2. Experimental setup

2.1 Bench-top system

In order to demonstrate the principles of high-speed 3D SEE, a bench-top system (Fig. 1) was constructed with parameters that approximated that of a 350 μm diameter endoscope. Images were obtained by using a mode locked titanium-sapphire laser (center wavelength 800 nm), with a

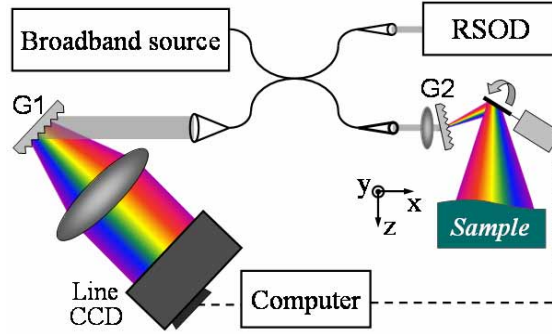


Fig. 1. Schematic of the spectrally-encoded imaging system. RSOD- rapidly scanning optical delay line; G1, G2 - diffraction gratings.

large spectral bandwidth (250 nm). The broadband laser light was coupled to the input port of a single-mode fiber optic Michelson interferometer, using a rapidly-scanning optical delay line (RSOD) [15] as the reference arm reflector to. In the sampling arm, a miniature endoscopic imaging probe was simulated by a compact lens-grating design in which the beam was first focused by a lens ($f = 40$ mm, beam diameter 0.35 mm) and then diffracted by a transmission grating (1000 lines/mm) to form a spectrally-encoded line (x-axis) on the surface of the sample. For this demonstration, a galvanometric beam scanner was used for slow (y) axis scanning. The transverse resolution was approximately $80\text{ }\mu\text{m}$ in each direction. The total optical power on the sample was 4 mW.

Axial resolution was accomplished with spectral-domain interferometry by using the bandwidth incident on each resolvable point in the transverse plane ($\delta z \cong 0.44\lambda^2 N_x / \Delta\lambda$). Every spectrally encoded line in the image contained $N_x \cong 120$ resolvable points (Eq. 1), each of which was illuminated with a bandwidth of $\delta\lambda \cong \Delta\lambda / N_x \cong 2.1$ nm, resulting in an axial resolution δz of approximately $135\text{ }\mu\text{m}$. Light from the sample and reference arms returned through the fiber optic interferometer and directed to a custom spectrometer with a spectral resolution of 0.1 nm, which resulted in a depth range of approximately 2.8 mm. Spectra were digitized using a high-speed line scan camera (Basler L104k-2k, 30 kHz line rate) and processed by a computer. Raw data was stored and images were displayed in real-time. The detection sensitivity was measured to be ~ 75 dB.

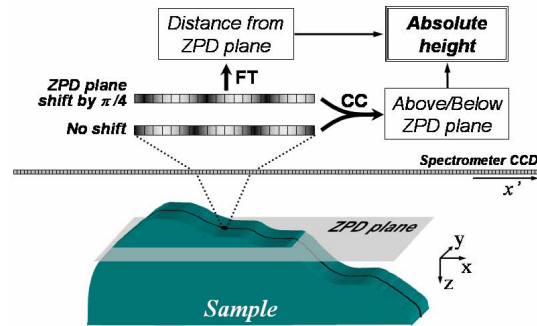


Fig. 2. Data capturing and processing schematic. ZPD - zero path difference. FT - Fourier transform. CC - cross correlation.

2.2 Data processing

The method of image acquisition and processing is illustrated schematically in Fig. 2. Each spectral band reflected from the sample interferes with the corresponding reference spectral

band on the line scan camera. The interference pattern has a spatial modulation frequency that is proportional to the axial distance of the point from an imaginary plane that matches the optical path length of the reference arm, which we term the 'zero path difference (ZPD) plane'. The location of the ZPD plane is determined by the RSOD position in the reference arm. The RSOD was also used to compensate for differences in dispersion between the sample and reference arms. Short-time Fourier transformation of the recorded signal enables determination of the distance for each point along the spectrally-encoded line.

Without further processing, there is an ambiguity as to whether the interrogated surface is above or below the ZPD plane. Thus, we utilized the RSOD to control the group delay of the reference arm light and remove depth ambiguity. The RSOD continuously varied the reference path length during acquisition resulting in a $\Delta\theta \cong \pi/2$ phase difference between adjacent lines [16]. Image data was over-sampled by capturing 5 spectrally-encoded lines per resolution element. One way of determining whether the surface is above or below the zero path difference plane is to calculate the difference between short-time Fourier transform (STFT) phases of adjacent lines:

$$p_{ij} = \text{sign}\left\{\text{angle}\left[FT\left(I_{i,j}\left(x'\right)\right)\right] - \text{angle}\left[FT\left(I_{i,j+1}\left(x'\right)\right)\right]\right\}, x' \in \left[\lambda_i^0 - \delta\lambda/2, \lambda_i^0 + \delta\lambda/2\right], \quad (2)$$

where x' denotes the horizontal coordinate of the raw data along the spectrally encoded line, and $I_{i,j}$ and $I_{i,j+1}$ are two adjacent windows i along one spectrally encoded line j , which is encoded by a bandwidth $\delta\lambda$ centered at λ_i^0 . We found this straightforward technique to be fast and easy to implement, however, it was very sensitive to the presence of noise, leading to a high error rate when the SNR was low. We therefore implemented a different approach, which included calculating the cross-correlation between each two adjacent windows (i,j) and ($i,j+1$),

$$C_{ij}(x') = \int_{\lambda_i^0 - \delta\lambda/2}^{\lambda_i^0 + \delta\lambda/2} I_{i,j}(\xi) I_{i,j+1}(\xi + x') d\xi. \quad (3)$$

Due to over-sampling along the y axis, the only difference between adjacent spectrally encoded lines is the interference pattern shift imposed by the small change of the reference arm:

$$I_{i,j+1}(x') = I_{i,j}(x' - \Delta\theta). \quad (4)$$

Substituting Eq. (4) into Eq. (3) yields:

$$C_{ij}(x') = \int_{\lambda_i^0 - \delta\lambda/2}^{\lambda_i^0 + \delta\lambda/2} I_{i,j}(\xi) I_{i,j}(\xi + x' - \Delta\theta) d\xi = A_{ij}(x' - \Delta\theta), \quad (5)$$

where A_{ij} is the autocorrelation of each window (i,j). Since A_{ij} has its maxima at its center coordinate $x' - \lambda_i^0$, $C_{ij}(x')$ is at a maximum at $x' = \lambda_i^0 - \Delta\theta$. Thus, calculating the location of the cross-correlation maxima

$$\Delta\theta_{ij} = \text{index}\left[\max\left(C_{ij}(x')\right)\right], \quad (6)$$

provides both the magnitude of the pattern shift, as well as its direction, which is positive for points above the ZPD and negative for those below. Eq. (6) can be used to obtain the depth information without ambiguity; however, it was less sensitive to the presence of noise than Eq. (2) in determining the absolute value of the height. As a result, in order to minimize data processing errors, we have used Eq. (2) to determine the surface height and Eq. (6) to remove height ambiguity.

2.3 Probe

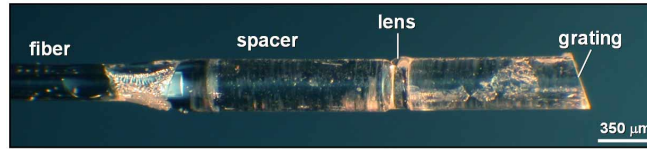


Fig. 3. A photograph of the distal optics of the SEE probe.

The first prototype miniature SEE probe [14] is depicted in Fig. 3. Light from a single-mode fiber (Corning HI 780), was expanded through a 1.8 mm long silica spacer and was then focused by a 350 μm diameter, 210 μm long GRIN lens. At the tip of the probe, the light was diffracted by a 1000 lines/mm transmission grating (Holographix LLC, Hudson, MA) that was fabricated on a 1.5 mm long spacer polished at Littrow's angle of 19° . Parts were assembled using optically clear epoxy with a refractive index matched to that of the micro-optics, thereby reducing reflections from optical interfaces. The maximum diameter of the probe was 350 μm . Since the probe was constructed from a single optical fiber, it was very flexible, with a bend radius of approximately 2 mm, except within ~ 3.5 mm of the rigid distal end. The prototype SEE probe had a field of view of approximately 2.6 mm, a lateral resolution of 30 μm FWHM, and a 10 mm working distance. The confocal parameter was approximately 3.6 mm, and the angular field of view (angle between the shortest and the longest wavelength) was 15° . Scanning along the axis perpendicular to the spectrally-encoded line was obtained by rotating the fiber that was attached to a galvanometer shaft, approximately 20 cm away from the distal end of the probe. The maximum rotation angle was 40° .

3. Results

A detailed, step-by-step, demonstration of the techniques used to unambiguously obtain 3D reconstructions with spectral-domain SEE is presented in Figs. 4-7. For this example we present and analyze raw data obtained from the face of a small plastic doll (Fig. 4, inset). The detection spectrometer was designed to obtain a spectral resolution of approximately 0.1 nm, 20 times higher than the spectral resolution provided by the SEE imaging optics in the sample arm. Background signal, measured by blocking the sample arm, was subtracted to enhance interference fringe contrast. The raw, background subtracted, interference image shown in Fig. 4 is comprised of 500 horizontal lines (j -axis) with 2048 pixels per spectrally-encoded line (x' axis).

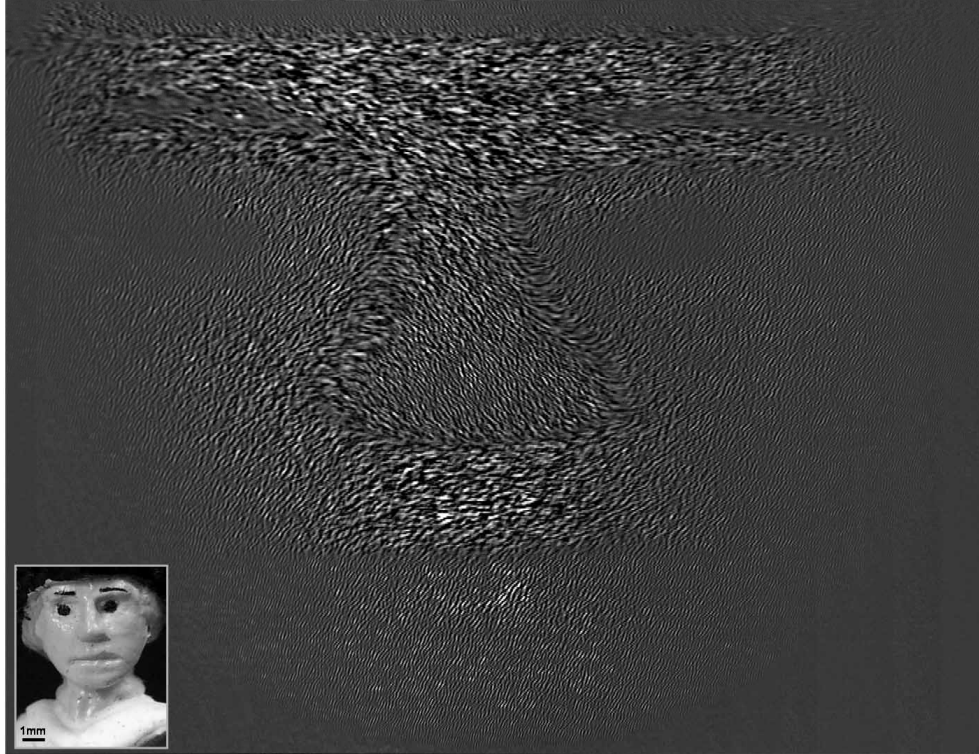


Fig. 4. Background subtracted raw fringe data obtained from the face of a plastic doll (inset).

An expanded region of the raw image taken from the area between the nose and the left eye reveals the interferometric patterns in more detail [Fig. 5(a)]. Intensity cross-sections along two adjacent horizontal lines marked by a solid line ($I_{i,j}$) and a dashed line ($I_{i,j+1}$) in Fig. 5(a), are shown in the top plot of Fig. 5(b). The corresponding power spectra are shown as solid and dashed lines in the lower left plots in Figs. 5(b). The cross-correlation between the two lines was calculated and is plotted in the lower right plot in Fig. 5(b). Note that the maximum of the cross-correlation trace is located at $x' < \lambda_i^0$, implying that this location is below the ZPD plane. Data processing from a different sample location is illustrated in Fig. 6. The intensity cross-section shows larger amplitude (due to higher reflectance), slightly higher spatial frequency (due to a larger distance from the ZPD plane) and a cross-correlation trace that peaks at $x' < \lambda_i^0$, indicating a location above the ZPD plane.

Data processing of the entire image involved the computation of STFT from each horizontal line I_j of the raw image using 256, partly overlapping, rectangular 32-pixel-wide windows. Depth unwrapping was obtained using Eq. (5) and Eq. (6) (256 windows, 32-pixel-wide). Note that the depth information can be determined by visual inspection of the raw image: Low spatial frequencies represent regions closer to the ZPD plane, which is located at the base of the nose, immediately above the upper lip. Also, areas that are lower (higher) than the ZPD plane show diagonal flow-like pattern from top-right (top-left) to the bottom-left (bottom-right).

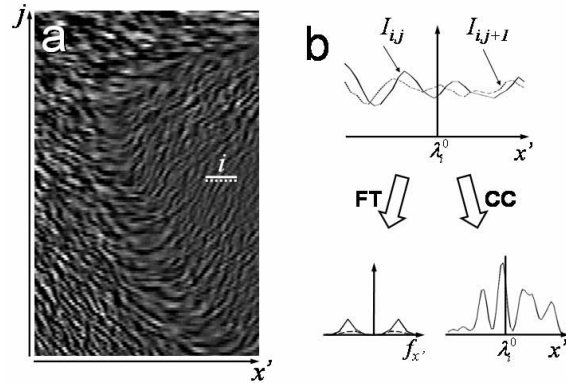


Fig. 5. (a). An expanded region of Fig. 4. (b). The intensity cross-sections along the solid and the dashed lines in (a), with its corresponding Fourier transformation and cross-correlation traces. FT - Fourier transform; CC - cross-correlation; $f_{x'}$ - spatial frequencies along x' .

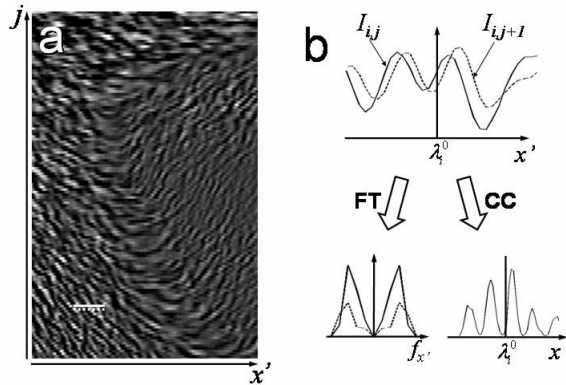


Fig. 6. (a). An expanded region of Fig. 4. (b). The intensity cross-sections along the solid and the dashed lines in (a), with its corresponding Fourier transformation and cross-correlation traces. FT - Fourier transform; CC - cross-correlation; $f_{x'}$ - spatial frequencies along x' .

An image, mapping the reflectance intensity from the doll's face, was obtained by calculating the logarithm of the maximum intensity value of each FT, and is shown in Fig. 7(a). This 2D image of the doll's face reveals regions of low reflectance such as the eyes, the eyebrows and the hat. Note the characteristic speckle pattern typical of coherent imaging. A height map of the doll's face, obtained by calculating the local spatial frequencies using STFT, is shown in Fig. 7(b). Note also that the depth dimension in this image is "folded" around the ZPD plane: the nose appears to have the same height as the eyes.

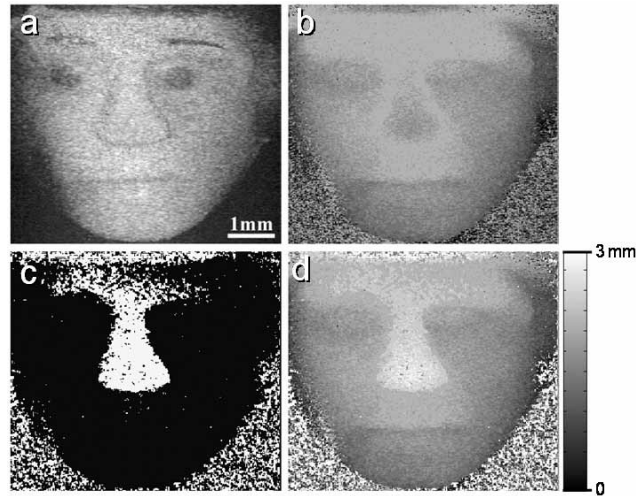


Fig. 7. (a). Calculated 2D reflectance image of the doll's face. (b). Height map demonstrating depth ambiguity around the base of the nose. (c). Sign map for unwrapping the depth image, obtained by calculating the maxima of the cross-correlation traces. (d). Unwrapped depth map. Imaging speed was 30 volumes per second.

The unwrapping $[\text{sign}(\Delta\theta_{ij})]$ matrix, shown in Fig. 7(c), was used to remove depth ambiguity by multiplying the image of Fig. 7(b) with that of Fig. 7(c) on a pixel by pixel basis. The resulting unwrapped height map, shown in Fig. 7(d), has two times greater depth range (20 resolvable points) than the unwrapped image (Fig. 7(b), 10 axial points). Since height can be determined at every point in the image that contains signal, the height image does not suffer from speckle noise as in the reflectance 2D image [Fig. 7(a)]. Compared with time-domain SEE, which was limited by the scanning range of the RSOD (1.5 mm) [13], here the depth range was approximately 2.8 mm, limited primarily by the spectrometer resolution.

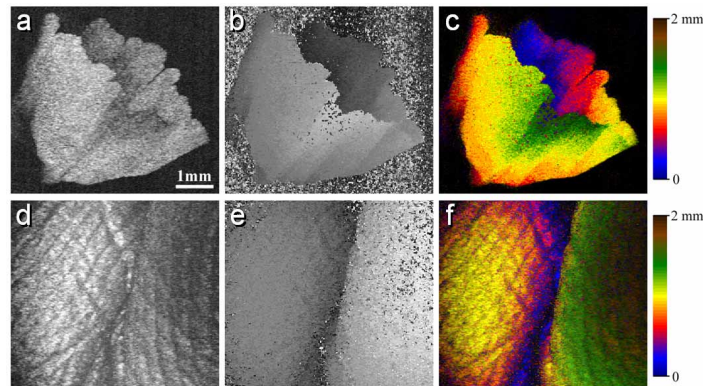


Fig. 8. (a). Two-dimensional image of a small paper flower. (b). Height map of the flower in (a). (c). 3D representation of the paper flower where height is superimposed on the reflectance image using a false color look-up table. (d). Two-dimensional image of a skin fold on volunteer's hand. (e). Height map of the skin fold in (d). (f). 3D representation of the skin fold where height is superimposed on the reflectance image using a false color look-up table. All images are presented at the same scale. Imaging speed was 30 volumes per second.

Two- and three-dimensional images obtained with the bench-top system are shown in Fig. 8. The imaging rate was 30 volumes per second; each volume comprises $80 \times 100 \times 20$ resolvable points, covering a field of view of approximately $2.5 \text{ mm} \times 2.5 \text{ mm} \times 3.2 \text{ mm}$ (x-y-

z, respectively). The galvanometric scanner of the RSOD (6210, Cambridge technologies Inc.) was driven at 30 Hz, scanning the reference arm optical path length over approximately 100 μm for each period. A two-dimensional reflectance image of a small paper flower is shown in Fig. 8(a). Surface height is represented by gray levels, where a high pixel value represents sample locations closer to the imaging lens [Fig. 8(b)]. Figure 8(c) shows the depth information superimposed on the reflectance 2D image where height is encoded by color. Figs. 8(d) – 8(f) depict images of a skin-fold on a volunteer's hand. Fine details can be visualized in the two-dimensional image of the skin fold [Fig. 8(d)], but the addition of the 3D information reveals the height difference between the right and the left parts of the image [Figs. 8(e), 8(f)].

To demonstrate the potential of the system for fetoscopy, we imaged the hind paws of a preserved mouse embryo (stage E18.5) inside a polypropylene 50 ml tube (2 mm thick plastic wall), through an approximately 10 mm thick layer of 3.7% formaldehyde fixative solution (Fig. 9). The two-dimensional image [Fig. 9(a)] is relatively nondescript, only showing the presence of two paws and the tail. Addition of 3D information [Figs. 9(b), 9(c)], however allows the identification of all five digits and their claws, as well as the paw's structure and its location in space relative to the tail and the second hind paw.

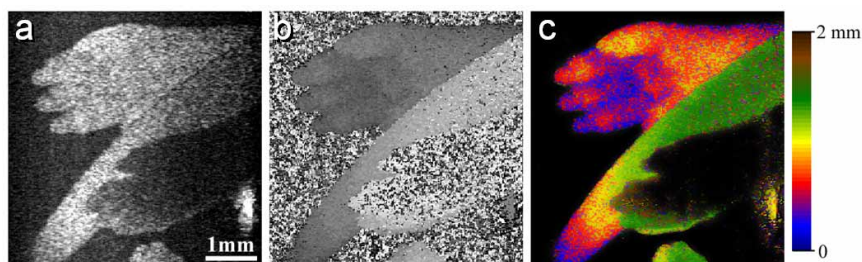


Fig. 9. (a). Two-dimensional image of the hind paws and tail of a mouse embryo. (b). Height map of (a). (c). 3D representation of the mouse hind paws where height is superimposed on the reflectance image using a false color look-up table. Black represents absence of two- and three-dimensional information owing to low reflectance. Imaging speed was 30 volumes per second.

These experiments demonstrate the feasibility of spectral-domain SEE to obtain video-rate 3D images through a single optical fiber. However, the true promise of SEE is only realized through miniature endoscopy. In a previous publication [14] we demonstrated preliminary *in vivo* 3D-SEE images of metastatic ovarian cancer tumor nodules. In Fig. 10 we demonstrate increased 3D-volumetric range by imaging human middle ear ossicles *ex vivo* with the SEE probe. This image clearly reveals the fine structure and spatial relationships of the malleus, incus, and stapes. In order to cover sufficient depth of field we acquired four volumetric data sets as the reference path length was changed in four 1.5 mm steps, without moving the probe. The combined data set covers a 5 mm x 5 mm x 6 mm field of view with 120 x 120 x 80 resolvable points (x-y-z, respectively). A photograph of the ossicles that were excised from a human left ear and reassembled to approximate their natural configuration is shown in the inset. We have found that the image quality obtained through the SEE probe was generally comparable to that obtained with the bench top system, with the exception of noticeable phase instabilities at high frame rate, caused by the rapid rotational motion of the probe. This phase noise mainly increased the error rate for removing depth ambiguity, resulting in some artifacts in the unwrapped image. Due to the small dimensions and the 3D capabilities of the SEE probe, minimally invasive imaging of the middle ear through a small incision in the tympanic membrane, a tympanostomy tube, or alternatively, by inserting the probe trans-nasally into the Eustachian tube could be realized. [17] 3D endoscopy of these and other anatomical structures might significantly aid physicians in the diagnosis and treatment of middle ear disorders.

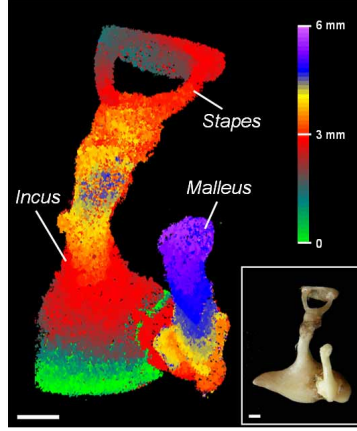


Fig. 10. 3D imaging of excised human ossicles using the SEE probe. The inferior view was imaged to highlight the incudostapedial joint (articulation of incus and stapes). The SEE image is displayed using a false color look-up table representing height. The inset depicts a photograph of the ossicles. Scale bars represent 1 mm.

4. SNR analysis

In its native form, [11] SEE can be performed using a CCD-based spectrometer that records backreflections from the sample. Having no reference arm, this approach can be used for imaging reflectance in 2D only. When the reflectivity from the sample is low, which is often the case for biomedical imaging, the electrical noise of the CCD camera is the dominant noise source. Assuming a uniformly flat spectrum, the SNR is given by $SNR_{2D} = n_{signal}^2 / n_{noise}^2$, where n_{noise} represents the number of noise electrons in each CCD pixel, and n_{signal} the number of signal electrons per pixel associated with the sample light. The number of signal electron is given by $n_{signal} = \eta R P_s \tau / (N_x h \nu)$, where η denotes the quantum efficiency of the spectrometer, R is the reflectivity of the sample, P_s is the total sample power, τ is the integration time (line scan period), N_x is the number of transverse resolvable points per line, and ν is the optical frequency. The SNR can be expressed as:

$$SNR_{2D} = \left(\frac{\eta R P_s \tau}{h \nu N_x n_{noise}} \right)^2. \quad (7)$$

With typical parameters, $n_{noise} = 170$, $N_x = 100$, $\tau = 166 \mu s$ (assuming 30 fps, 200 lines per image), $P_s = 0.1$ mW, and $\eta = 0.5$, the minimum detectable reflectivity corresponding to $SNR_{2D} = 1$ is $R = 5.1 \times 10^{-7}$ at approximately 800 nm.

In time-domain SEE, [13] light reflected from the sample is combined with reference light in a Michelson interferometer employing a scanning delay line. An STFT of the interference signal is recorded with a photodiode, producing a 3D image. Assuming a shot-noise limited detection, the SNR associated with a particular spatial point with reflectivity R is given by:

$$SNR_{TD} = \frac{2\eta \frac{P_r}{N_x} R \frac{P_s}{N_x}}{2h\nu B P_r} = \frac{2\eta R P_s \tau}{h\nu N_x^2 N_z}, \quad (8)$$

where P_r denotes the total reference power, N_z the number of axial resolvable points per spectrally-encoded line, and $B = N_z / (2\tau)$ is the measurement bandwidth. Note that SNR_{TD} is inversely proportional to the square of the number of transverse resolvable points since only a fraction of the reference arm power (P_r / N_x) interferes with the light returning from a single transverse location. With $N_x = 100$, $N_z = 10$, $\tau = 1$ ms (5 fps, 200 lines per image), and $P_s = 0.1$ mW, the minimum detectable reflectivity is determined to be $R = 2.5 \times 10^{-7}$ at approximately

800 nm. In previous experiments with time-domain SEE we found that the typical SNR for imaging tissue was 6-10 dB. [13]

In the spectral-domain SEE presented in this work, the SNR is given by:

$$SNR_{SD} = \frac{2\eta \frac{P_r}{N_x} R \frac{P_s}{N_x}}{2h\nu B(P_r/N_x)} = \frac{2\eta R P_s \tau}{h\nu N_x}, \quad (9)$$

where $B=1/(2\tau)$ is the measurement bandwidth. It is clear from (8) and (9) that, with all parameters being equal, the spectral domain approach offers a SNR advantage by a factor $N_x N_z$. The improvement factor is equal to the total number of resolvable points, which is 2000 in our experimental system.

With $N_x = 100$, $\tau = 67 \mu s$ (30 fps, 200 lines per image, 3x over-sampling factor), and $P_s = 0.1$ mW, the minimum detectable reflectivity is $R = 4.44 \times 10^{-9}$ at 800 nm, corresponding to a sensitivity of 83 dB. Typical SNR for tissue imaging demonstrated in this work was 30-35 dB. A sensitivity of 77 dB, 6 dB short of the theoretical shot-noise limit due to losses in the spectrometer, was measured by calculating the ratio between the signal from a mirror through a neutral density filter and the image noise floor.

5. Discussion

Compared to previously published time-domain techniques, [11, 13] spectral-domain SEE allows 3D imaging with approximately 2 orders of magnitude higher SNR, more than 5-fold increase in imaging speed, and 2-fold increase in depth range in a single capture. Due to its high sensitivity (77 dB), imaging speed is limited only by the spectrometer's camera line rate. With our camera, volumetric imaging was possible at video rates. The depth range in a single capture depends on the ratio between the spectral resolution of the probe and the spectrometer. The spectrometer resolution is a fundamental limitation of this single-capture scheme. It is, however, possible to increase this range by stepping the reference path length and acquiring another spectral dataset. With this method, which doesn't require any movement of the probe and can be performed rapidly using the RSOD, the depth range can be increased significantly, as is demonstrated in Fig. 10, where four spectral captures corresponding to four different locations of the reference arm were added to get a total depth range of 6 mm.

Our combination of the spectral-domain detection scheme with the newly-developed miniature imaging probe [14] has the potential to offer unique capabilities to physicians and surgeons. Minimized tissue damage and the reduced need for anesthesia provided by such a small endoscope may allow many diagnostic and minor surgery procedures to be conducted in the outpatient setting. For example, procedures such as assessment and treatment of pelvic adhesions, tubal sterilization, and fertilization, might be more easily conducted with SEE under local anesthesia. [18-20] The SEE probe may also allow safer navigation through delicate intraluminal structures such as the salivary ducts, [21] the fallopian tube, [22] and pancreatic duct [23]. Fetal and pediatric procedures could benefit from this tool as well, including fetoscopy, fetoscopic surgery, and pediatric surgery. [6, 24, 25] The effectiveness of recently introduced minimally invasive techniques, such as mammary ductoscopy, [3, 4] neuroendoscopy, [26] microendoscopic discectomy [27] and coronary angioscopy, [2, 28] may also be greatly improved by the introduction of flexible, 3D imaging probes with small diameters.

Some challenges remain before the promise of SEE can be fully realized. Navigation mechanisms should be implemented with minimal additional bulk and without compromising flexibility. SEE probes can be designed for forward viewing and can have up to 55° viewing angle with a wide range of working distances and fields of view. For applications that require even smaller dimensions, SEE probes as small as 125 μm in diameter may be fabricated with a sufficiently high number of pixels for clinical imaging. Speckle noise, resulting from the coherent nature of the illuminating light and manifested in the two-dimensional SEE images as a grainy appearance, can be removed using a dual-clad fiber geometry [29]. Color, required

for some applications, can be implemented using three separate broad bandwidth sources, each centered at visible red, green, and blue wavelengths. SEE of fluorescence light can also be utilized [30] for molecular imaging.

Acknowledgments

This study was funded in part by the Center for Integration of Medicine and Innovative Technology, and a National Science Foundation grant (BES-0086709). The authors thank Dr. Mei Wu for supplying the mouse embryos and Dr. Parviz Janfaza for providing the middle ear samples.